

GTC Follow-up Observations of Very Metal-Poor Star Candidates from DESI

CARLOS ALLENDE PRIETO,^{1,2} DAVID S. AGUADO,^{1,2,3} JONAY I. GONZÁLEZ HERNÁNDEZ,^{1,2} RAFAEL REBOLO,^{1,4,2} JOAN NAJITA,⁵ CHRISTOPHER J. MANSER,⁶ CONSTANCE ROCKOSI,^{7,8} ZACHARY SLEPIAN,⁹ MAR MEZCUA,^{10,11} MONICA VALLURI,¹² RANA EZZEDDINE,¹³ SERGEY E. KOPOSOV,^{14,15} ANDREW P. COOPER,^{16,17,18} ARJUN DEY,⁵ BORIS T. GÄNSICKE,¹⁹ TING S. LI,²⁰ KATIA CUNHA,²¹ SIWEI ZOU,²² JESSICA NICOLE AGUILAR,⁹ STEVEN AHLEN,²³ DAVID BROOKS,²⁴ TODD CLAYBAUGH,⁹ SHAUN COLE,²⁵ SARAH EFTEKHARZADEH,²⁶ KEVIN FANNING,²⁷ JAIME FORERO-ROMERO,²⁸ SATYA GONTCHO A GONTCHO,⁹ KLAUS HONSCHEDT,^{29,30,27} PASCALE JABLONKA,³¹ ROBERT KEHOE,³² THEODORE KISNER,⁹ MARTIN LANDRIAU,⁹ AXEL DE LA MACORRA,³³ AARON MEISNER,³⁴ RAMÓN MIQUEL,^{35,36} JOHN MOUSTAKAS,³⁷ JUNDAN NIE,³⁸ CLAIRE POPPETT,^{9,39,40} FRANCISCO PRADA,⁴¹ MEHDI REZAIE,⁴² GRAZIANO ROSSI,⁴³ EUSEBIO SÁNCHEZ,⁴⁴ MICHAEL SCHUBNELL,^{45,46} RAY SHARPLES,^{47,25} MALGORZATA SIUDEK,¹⁰ VERNE V. SMITH,⁵ GREGORY TARLÉ,⁴⁶ FIORENZO VINCENZO,^{48,27} BENJAMIN ALAN WEAVER,³⁴ ZHIMIN ZHOU,³⁸ AND HU ZOU³⁸

¹*Instituto de Astrofísica de Canarias, Vía Láctea, 38205 La Laguna, Tenerife, Spain*

²*Universidad de La Laguna, Departamento de Astrofísica, 38206 La Laguna, Tenerife, Spain*

³*Dipartimento di Fisica e Astronomia, Università degli Studi di Firenze, Via G. Sansone 1, I-50019 Sesto Fiorentino*

⁴*Consejo Superior de Investigaciones Científicas*

⁵*NSF's NOIRLab, 950 N. Cherry Ave., Tucson, AZ 85719, USA*

⁶*Imperial College London, South Kensington Campus, London SW7 2AZ, UK*

⁷*Department of Astronomy and Astrophysics, University of California, Santa Cruz, 1156 High Street, Santa Cruz, CA 95065, USA*

⁸*University of California Observatories, 1156 High Street, Santa Cruz, CA 95065, USA*

⁹*Lawrence Berkeley National Laboratory, 1 Cyclotron Road, Berkeley, CA 94720, USA*

¹⁰*Institute of Space Sciences, ICE-CSIC, Campus UAB, Carrer de Can Magrans s/n, 08913 Bellaterra, Barcelona, Spain*

¹¹*Institut d'Estudis Espacials de Catalunya (IEEC), 08034 Barcelona, Spain*

¹²*Department of Astronomy, University of Michigan, Ann Arbor, MI 48109, USA*

¹³*Department of Astronomy, University of Florida, 211 Bryant Space Science Center, P.O. Box 112055, Gainesville, FL 32611-2055, USA*

¹⁴*Institute for Astronomy, University of Edinburgh, Royal Observatory, Blackford Hill, Edinburgh EH9 3HJ, UK*

¹⁵*Institute of Astronomy, University of Cambridge, Madingley Road, Cambridge CB3 0HA, UK*

¹⁶*Institute of Astronomy and Department of Physics, National Tsing Hua University, 101 Kuang-Fu Rd. Sec. 2, Hsinchu 30013, Taiwan*

¹⁷*Center for Informatics and Computation in Astronomy, NTHU, 101 Kuang-Fu Rd. Sec. 2, Hsinchu 30013, Taiwan*

¹⁸*Physics Division, National Center for Theoretical Sciences, Taipei 10617, Taiwan*

¹⁹*Department of Physics, University of Warwick, Gibbet Hill Road, Coventry, CV4 7AL, UK*

²⁰*Department of Astronomy & Astrophysics, University of Toronto, Toronto, ON M5S 3H4, Canada*

²¹*Steward Observatory, University of Arizona, 933 N, Cherry Ave, Tucson, AZ 85721, USA*

²²*Department of Astronomy, Tsinghua University, 30 Shuangqing Road, Haidian District, Beijing, China, 100190*

²³*Physics Dept., Boston University, 590 Commonwealth Avenue, Boston, MA 02215, USA*

²⁴*Department of Physics & Astronomy, University College London, Gower Street, London, WC1E 6BT, UK*

²⁵*Institute for Computational Cosmology, Department of Physics, Durham University, South Road, Durham DH1 3LE, UK*

²⁶*Universities Space Research Association, NASA Ames Research Centre*

²⁷*The Ohio State University, Columbus, 43210 OH, USA*

²⁸*Departamento de Física, Universidad de los Andes, Cra. 1 No. 18A/10, Edificio Ip, CP 111711, Bogotá, Colombia*

²⁹*Center for Cosmology and AstroParticle Physics, The Ohio State University, 191 West Woodruff Avenue, Columbus, OH 43210, USA*

³⁰*Department of Physics, The Ohio State University, 191 West Woodruff Avenue, Columbus, OH 43210, USA*

³¹*Ecole Polytechnique Fédérale de Lausanne, CH-1015 Lausanne, Switzerland*

³²*Department of Physics, Southern Methodist University, 3215 Daniel Avenue, Dallas, TX 75275, USA*

³³*Instituto de Física, Universidad Nacional Autónoma de México, Cd. de México, C.P. 04510, México*

³⁴*NSF's NOIRLab, 950 N. Cherry Ave., Tucson, AZ 85719, USA*

³⁵*Institució Catalana de Recerca i Estudis Avançats, Passeig de Lluís Companys, 23, 08010 Barcelona, Spain*

³⁶*Institut de Física d'Altes Energies (IFAE), The Barcelona Institute of Science and Technology, Campus UAB, 08193 Bellaterra Barcelona, Spain*

³⁷*Department of Physics and Astronomy, Siena College, 515 Loudon Road, Loudonville, NY 12211, USA*

³⁸*National Astronomical Observatories, Chinese Academy of Sciences, A20 Datun Rd., Chaoyang District, Beijing, 100012, P.R. China*

³⁹*Space Sciences Laboratory, University of California, Berkeley, 7 Gauss Way, Berkeley, CA 94720, USA*

⁴⁰*University of California, Berkeley, 110 Sprout Hall #5800 Berkeley, CA 94720, USA*

⁴¹*Instituto de Astrofísica de Andalucía*

⁴²*Department of Physics, Kansas State University, 116 Cardwell Hall, Manhattan, KS 66506, USA*

⁴³*Department of Physics and Astronomy, Sejong University, Seoul, 143-747, Korea*

⁴⁴*CIEMAT, Avenida Complutense 40, E-28040 Madrid, Spain*

⁴⁵*Department of Physics, University of Michigan, Ann Arbor, MI 48109, USA*

⁴⁶*University of Michigan, Ann Arbor, MI 48109, USA*

⁴⁷*Centre for Advanced Instrumentation, Department of Physics, Durham University, South Road, Durham DH1 3LE, UK*

⁴⁸*E.A. Milne Centre for Astrophysics, University of Hull, Hull, HU6 7RX, United Kingdom*

(Received June 13, 2023)

ABSTRACT

The observations from the Dark Energy Spectroscopic Instrument (DESI) will significantly increase the numbers of known extremely metal-poor stars by a factor of ~ 10 , improving the sample statistics to study the early chemical evolution of the Milky Way and the nature of the first stars. In this paper we report high signal-to-noise follow-up observations of 9 metal-poor stars identified during the DESI commissioning with the Optical System for Imaging and low-Intermediate-Resolution Integrated Spectroscopy (OSIRIS) instrument on the 10.4 m Gran Telescopio Canarias (GTC). The analysis of the data using a well-vetted methodology confirms the quality of the DESI spectra and the performance of the pipelines developed for the data reduction and analysis of DESI data.

Keywords: stars: PopulationII – stars: abundances – stars: PopulationIII – Galaxy:abundances – Galaxy:formation – Galaxy:halo

1. INTRODUCTION

Only hydrogen, helium, and traces of lithium nuclei were formed in primordial nucleosynthesis, completed 20 minutes after the Big Bang. Lithium and beryllium formed later in substantial amounts from spallation processes between helium, carbon, nitrogen, oxygen nuclei and cosmic rays, but heavier elements come mainly from burning in stars or explosive nucleosynthesis. When the first stars formed 300 – 500 Myr after the Big Bang, they were made out of pristine gas, unpolluted by metals.

Simulations show that making stars from zero-metallicity molecular clouds is challenging (e.g. Greif et al. 2011; Stacy & Bromm 2014). The fragmentation and collapse of the clouds is greatly enhanced by radiative cooling from carbon and oxygen atoms, unavailable for the first generation of stars (Bromm & Larson 2004). This was thought to lead to a top-heavy stellar mass function, missing entirely the low-mass stars that may survive until today (Clark et al. 2011). Searches for very low metallicity stars prior to 2010 had provided very few objects at metallicities lower than $[\text{Fe}/\text{H}] = -4$ (Norris et al. 2013), i.e. 10,000 times less iron than in the Sun, in all cases with extremely large carbon enhancements that favored radiative cooling.

In 2011 a star was discovered with an iron abundance $[\text{Fe}/\text{H}] = -5$ but a solar carbon-to-iron ratio (Caffau et al. 2011). This object demonstrated that star formation calculations predicting it was not possible to form low-mass stars with a global metallicity $[\text{Z}/\text{H}] < -4$ (e.g. Bromm & Loeb

2003; Frebel et al. 2007) might be inaccurate. Since then a second example with very similar chemistry has been found (Starkenburg et al. 2018), and multiple theories have been proposed for the formation of low-mass stars from clouds with no metals (e.g. Stacy et al. 2016). A single supernova event can pollute a volume with a radius of 10 pc to $[\text{Fe}/\text{H}] \sim -3$ (Bertran de Lis et al. 2016). Lower metallicities are possible for lower gas densities than the typical values found in molecular clouds, an asymmetric supernova explosion, or mass fall-back onto a leftover black hole. Fall-back, in particular, can explain the extreme abundances of carbon in the most metal-poor stars (e.g. Umeda & Nomoto 2003; Iwamoto et al. 2005; Joggerst et al. 2009).

The chemical abundances of the most metal-poor stars give us critical information on the nucleosynthetic yields for the first stars and their supernovae, as well as on the early stages of assembly of the Galaxy and its chemical evolution. But given the vast volume and limited mixing in the interstellar medium in those early phases, a significant spread is expected and therefore it is essential to build a significant sample of extremely metal-poor (EMP) stars, and in particular those with the lowest metallicities. The majority of extremely metal-poor stars associated with the Milky Way are expected to be part of the stellar halo population (see, e.g. Starkenburg et al. 2017; Chen et al. 2023). Therefore, wide area high-galactic latitude surveys are most efficient at enlarging our samples.

There are only $\simeq 10$ stars known at $[\text{Fe}/\text{H}] \leq -5$, and roughly half of them were identified with data from the Sloan

Digital Sky Survey (SDSS; York et al. 2000). Other surveys such as RAVE (Kunder et al. 2017) or LAMOST (Cui et al. 2012), with samples of millions of stars, have contributed significant numbers of metal-poor stars, but are not particularly suited for exploring the most metal-poor domain. These will be enhanced by new projects such as the ongoing GALAH (Buder et al. 2020; Da Costa et al. 2022) and Gaia RVS (Gaia Collaboration et al. 2022), or the upcoming WEAVE (Jin et al. 2022) and 4MOST (de Jong et al. 2022) surveys. In addition to these, the Dark Energy Spectroscopic Instrument (DESI), pursuing a 5-year survey with a primary focus on cosmology (Levi et al. 2013), is now building a spectroscopic database that will soon exceed in size those from all its predecessors (DESI Collaboration et al. 2016a,b, 2022a). While the DESI survey focuses mainly on cosmological studies, a component of the bright time survey is dedicated to observations of Milky Way targets (Allende Prieto et al. 2020; Cooper et al. 2023). Based on the yields from the SDSS, we can expect the DESI survey by 2024 to increase the number of known stars with $[\text{Fe}/\text{H}] \leq -5$ by an order of magnitude.

The commissioning of DESI took place between 2019 and 2020, split into two phases separated by a shutdown caused by the COVID-19 pandemic. After Survey Validation, the DESI survey began in May 2021. As of this writing over 20 million spectra of galaxies and stars have been gathered by DESI and the observations continue at a good pace. A number of metal-poor stars observed during the commissioning phase were identified for follow-up with Gran Telescopio Canarias (GTC). The purpose of these observations was to check the data quality and the performance of the DESI data reduction and analysis pipelines with high signal-to-noise data obtained using a well-known instrumental setup and data analysis procedures. In this paper we report on these observations and compare the results from the two instruments.

2. DESI TARGETS

The DESI focal plane is set at the primary focus of the historic 4 m Mayall Telescope at Kitt Peak National Observatory. The focal plane has a field-of-view roughly 3.2 degrees in diameter (DESI Collaboration et al. 2022b), populated by 5000 robotic positioners that lead as many fibers to the desired target positions (Silber et al. 2023). These fibers feed 10 identical spectrographs, each with three cameras B, R and Z, covering between 360–580 nm, 576–762 nm, and 752–982 nm, respectively, at a FWHM resolution of about 0.18 nm (or a resolving power $R \equiv \lambda/\text{FWHM}(\lambda)$ of about 2000 on the blue edge, increasing to nearly 6000 at the red end). A detailed description of the instrument and the experiment can be found in the papers cited above, supplemented by several others already published or in preparation (Miller et al. 2022; Zou et al. 2017; Dey et al. 2019; Guy et al. 2023; Schlegel et

al. 2023; Bailey et al. 2023; Raichoor et al. 2023; Schlafly et al. 2023).

The DESI survey prioritizes the mapping of the redshift distribution of luminous galaxies and quasars. When observing conditions make this unachievable (e.g. when the moon is bright) the focus changes to nearby galaxies and stars. The DESI target selection is based on the public Legacy Surveys (Dey et al. 2019). Preliminary target selection details were published in 2020 (Allende Prieto et al. 2020; Ruiz-Macias et al. 2020; Zhou et al. 2020; Raichoor et al. 2020; Yèche et al. 2020), and several updates are available (Cooper et al. 2023; Hahn et al. 2022; Zhou et al. 2023; Raichoor et al. 2023; Chaussidon et al. 2023). A discussion of the data quality as assessed from visual inspection can be found in Lan et al. (2022); Alexander et al. (2022). The DESI Early Data Release (DESI collaboration et al. 2023) and the Siena Galaxy Atlas (Moustakas et al. 2022) are now publicly available.

The DESI stellar bright-time program is known as the Milky Way Survey (Cooper et al. 2023). Additional stellar spectra are associated to spectrophotometric calibrators (F- and A-type stars, plus white dwarfs), and the Backup program, which focuses on stars $g < 16$ and is active when the survey speed degrades significantly due to poor observing conditions, including morning and evening twilight. There are as well some secondary programs including stars approved by the DESI collaboration. The commissioning data discussed in this paper were obtained under a wide range of conditions and in some cases when the instrument was not fully functional, but the observations discussed here can be considered as representative of the range in the main survey.

Observing time on GTC was requested for 10 metal-poor stars with $g \sim 16$ at high spectral resolution using HORuS (Allende Prieto 2021, with a resolving power $R \sim 25,000$) and 9 fainter stars with $g \sim 17 - 18$ at lower resolution with OSIRIS¹ (Cepa 2010, $R \sim 2400$) selected among the most metal-poor stars in the commissioning data. Only the OSIRIS fraction of the requested time was granted and these are the stars discussed in this paper. The sample of OSIRIS/GTC observed stars provides a good benchmark to test the performance of the various versions of the DESI stellar pipelines.

Our sample is given in Table 1 and consists of 9 stars, plus the ultra metal-poor star J1313–0019 (Allende Prieto et al. 2015a), with $[\text{Fe}/\text{H}] \sim -5$, which was not observed by DESI but was nonetheless included in the OSIRIS sample to get a solid reference for the atmospheric parameters inferred from this instrument. In Fig. 1 we show in blue 6 DESI spec-

¹ Optical System for Imaging and low-Intermediate-Resolution Integrated Spectroscopy

Name/ DESI target ID	RA(deg)	DEC(deg)	g(mag)	Texp(s)	S/N@450 nm	Teff (K)	logg	[Fe/H]	[C/Fe]	RV (km s ⁻¹)
J1313-0019	198.362018	-0.32817	16.4	3 × 1350	168	5294	1.0	-5.03	3.77	263.9 ± 15
39627757558173121	180.676872	-1.23083	17.5	3 × 1200	100	5857	5.0	-2.89	0.51	35.8 ± 15
39627787731995518	179.145769	-0.08047	18.2	6 × 1200	85	5538	1.0	-3.25	2.02	-107.0 ± 15
35186036195721514	133.137090	11.39200	18.0	6 × 1000	140	6331	5.0	-3.64	1.80	-2.7 ± 15
35186077543172120	133.380322	13.22537	16.8	4 × 900	89	4652	5.0	-3.34	-0.04	305.8 ± 15
35186313011398455	157.980376	23.47101	18.2	3 × 1200	80	6438	5.0	-2.83	2.40	76.1 ± 15
35186395165230796	168.464724	27.22502	18.1	6 × 1200	125	6395	5.0	-2.93	<1.0	29.7 ± 15
39628465179202835	196.004469	29.29881	17.9	6 × 800	78	4666	4.2	-3.46	0.23	-47.4 ± 15
39633286363875367	214.592028	52.51449	18.3	6 × 1400	78	5920	3.8	-2.86	<1.00	-68.8 ± 15
39633315233267986	216.459371	54.39352	18.2	6 × 1200	121	6351	5.0	-2.75	0.79	-118.6 ± 15

Table 1. Stars observed for this program with OSIRIS on GTC, and their inferred atmospheric parameters (see text).

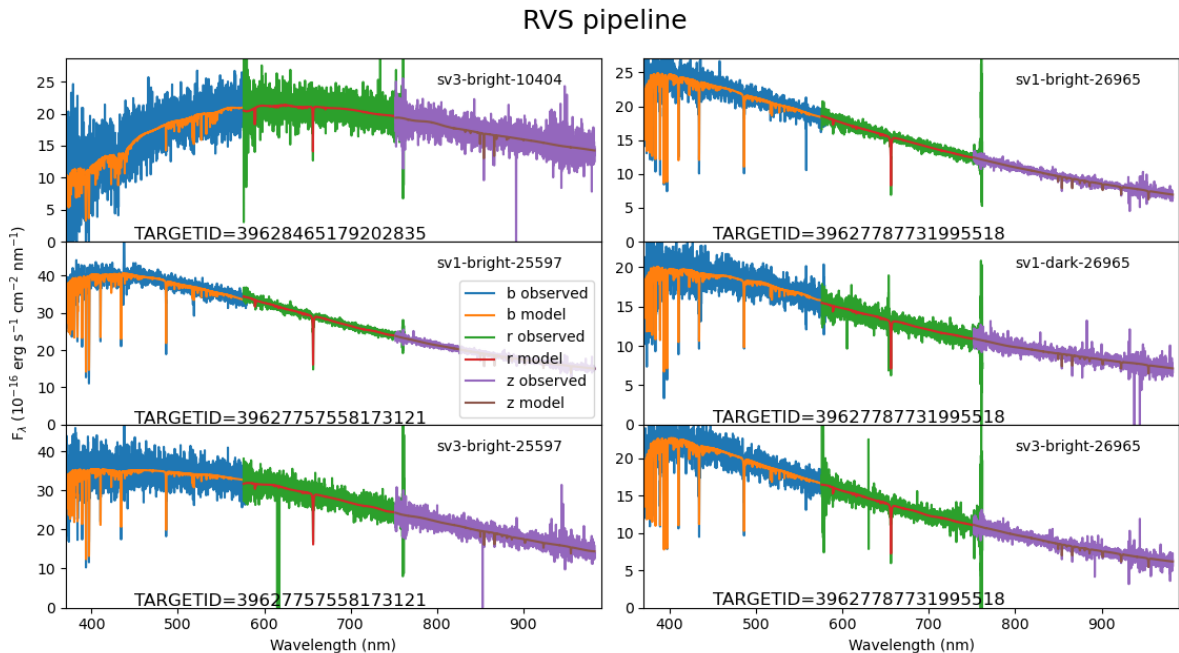


Figure 1. The DESI spectra of three of the candidates in our sample (blue lines) and the best fits (red) from the RVS pipeline. Two of the targets have been observed more than once, under different conditions or target selection schemes. The numerical DESI target identifications are indicated, as well as the survey (sv1 or sv3 stand for the first and third phases of the Survey Validation), observing conditions or program (bright/dark sky), and healpix number (Górski & et al. 1999).

tra of 3 of the stars studied. Two of these targets have been observed more than once under different conditions or target selections. The top-left panel corresponds to DESI target ID 39628465179202835, the middle and bottom left-hand panels correspond to target 39627757558173121, and the three right-hand panels to 39627787731995518. The red lines correspond to the best-fitting models from the DESI Milkyway Survey RVS pipeline, optimized to derive radial velocities for DESI data. Fig. 2 shows the same spectra, continuum normalized as analyzed by the SP pipeline, optimized for the

determination of chemical abundances, and the best-fitting models from this pipeline, limited to the 370–450 nm region to facilitate visual inspection. These two pipelines are described in more detail in Section 5 and in the overview paper by Cooper et al. (2023).

3. OSIRIS OBSERVATIONS

The OSIRIS spectrograph mounted on the 10.4 m GTC at the Roque de los Muchachos Observatory in La Palma, Canary Islands, was used in longslit mode over the period

19th–24th January 2021. The setup adopted grating 2500U, covering the 344 – 461 nm range, a 1.0 arcsec slit, and 2×2 binning, leading to a resolving power of $R \sim 2400$. The detector was the default device CCD1 + CCD2_A. To facilitate the removal of cosmic rays several exposures between 900 and 1400 s were taken for each object (See Table 1). As already mentioned, we also observed the hyper metal-poor star J1313–0019 (Allende Prieto et al. 2015b; Frebel et al. 2015). In total this program, 87-MULTIPLE-2/2, was completed in 15 hours. Data reduction was performed with the onedspec package within IRAF. Bias and flatfield correction, extraction, sky subtraction, and wavelength calibration were performed in the standard way by using HgAr, Ne, and Xe calibration lamps. All the spectra were corrected for barycentric velocity calculated with rvcorrect.

4. ANALYSIS OF THE OSIRIS-GTC OBSERVATIONS

4.1. Radial velocities

To derive radial velocities (RVs) an OSIRIS spectrum of G64–12, a well-known metal-poor star analysed in Aguado et al. (2017a), with $T_{\text{eff}} = 6393$ K, $\log g = 4.8$, $[\text{Fe}/\text{H}] = -3.2$, $[\text{C}/\text{Fe}] = +1.0$, was used as a template. First, we used the IRAF task `fxcor` we computed the Cross Correlation Function (CCF) for each individual spectra. Using these first estimates of the RV of each individual spectra we computed an average spectrum of each star which was subsequently analysed with a grid of models to derive the best fit stellar parameters and metallicity (see Section 4.2).

Due to the variety of stellar temperatures in our sample, ranging from about 4650 K to 6440 K, we decided to use the best-fitting FERRE synthetic spectra as templates to recompute the RV of each individual spectrum (see Fig. 3). To do that we used our own IDL-based automated code, which normalizes both the synthetic and observed OSIRIS spectra using a running mean filter with a width of 30 pixels. The CCF was built using almost the whole OSIRIS spectral range in the current setup from 3760 to 4450 Å with a window of 2000 km s⁻¹, in a similar manner to (Arentsen et al. 2023). The CCF has a similar shape as those of the strong features of the OSIRIS medium resolution spectra such as the H I Balmer lines, the Ca II H and K lines and the CH G-band with the adopted normalization procedure, which gives an oscillating pattern at the continuum of the CCF distinct from a Gaussian shape. To fit the whole CCF profile we employed a Gaussian model plus a second-order polynomial function. We finally derived the RV from a parabolic fit using the closest six points to the CCF peak.

The statistical uncertainty of the centroid of the parabolic fit is typically under 1 km s⁻¹, significantly below the pixel size of ~ 0.57 Å/pixel (~ 42 km s⁻¹). We also applied a running median filter that minimizes the oscillating pattern and allows a better fit of the CCF using a Gaussian,

although in this case we also adopted the parabolic fit of the CCF peak. Using the mean or the median normalization schemes provides differences under 1.5 km s⁻¹ for the parabolic fits, and under 3 km s⁻¹ for the Gaussian fits, respectively. The OSIRIS spectra do not include any telluric or sky lines useful to correct for instrument variability. The results of the OSIRIS spectra show intra-night RV variations with standard deviations in the range 6.5 – 15 km s⁻¹, and RV variations from different nights with standard deviations in the range 4 – 17 km s⁻¹. Therefore, we adopted an RV uncertainty floor of 15 km s⁻¹ to the RV uncertainties, which may reflect the systematic RV uncertainty due to instrument flexures, pointing, guiding RV drifts, etc. We provide the final derived RVs from the weighted mean of the individual RVs of each target using the normalization with a running median filter in Table 1. We note that the RV of the target SDSS J1313–0019 is consistent with the recent accurate RV of 273.984 ± 0.054 km s⁻¹ derived using the ESPRESSO spectrograph (Aguado et al. 2022).

4.2. Stellar parameters and metallicities

To derive stellar parameters, i.e., effective temperature (T_{eff}), surface gravity ($\log g$), overall metallicity ($[\text{Fe}/\text{H}]$) and carbon-to-iron ratio ($[\text{C}/\text{Fe}]$), we used the FERRE code (Allende Prieto et al. 2006a) and followed the methodology described in Aguado et al. (2016, 2017a,b). We employed two similar libraries of stellar spectra spanning slightly different stellar parameter ranges (Aguado et al. 2017b; Arentsen et al. 2020) computed with the ASSET code (Koesterke et al. 2008) and Kurucz model atmospheres (Mészáros et al. 2012). In these libraries a constant value $[\alpha/\text{Fe}] = +0.4$ is assumed, which reduces the number of free parameters to four. This approximation is helpful, given that the information that can be obtained at this modest resolution for very metal-poor stars is limited, and at the same time is valid for the vast majority of metal-poor stars in the Galaxy.

The grids of synthetic spectra were smoothed to the OSIRIS resolution ($R \sim 2400$). Then we normalized both the data and the grids, with a running mean filter of 25 pixels. FERRE is able to find the best fit by using the Boender-Timmer-Rinnoy-Kan (BTRK) algorithm (Boender et al. 1982) interpolating between nodes of the grids to derive the best set of values. Both grids are basically the same but one of them goes down to metallicity $[\text{Fe}/\text{H}] = -6$ and is suitable for ultra metal-poor stars like SDSS J1313–0019. Despite the high quality of the OSIRIS data it is not always possible to derive reliable $[\text{C}/\text{Fe}]$ at this resolution. Stellar parameters and carbon abundance play an important role here. This issue is deeply investigated in Aguado et al. (2019b) and we use the sensitivity curves they published and discriminate between reliable values and upper-limits. The results of this analysis are summarized in Table 1.

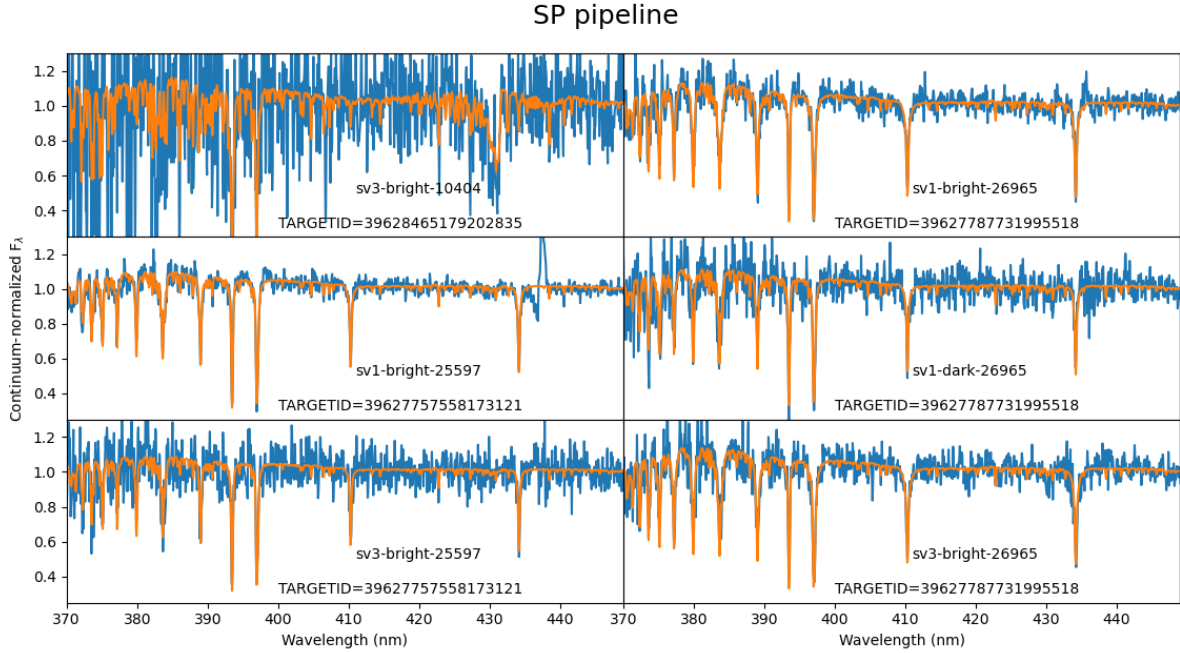


Figure 2. The continuum-normalized spectra of the same stars in Figure 1 (blue lines) and the best fits (red) from the SP pipeline, limited in this case to the 375–450 nm region.

The derived uncertainties ($\Delta T_{\text{eff}} = \pm 120$ K; $\Delta \log g = \pm 0.6$; $\Delta [\text{Fe}/\text{H}] = \pm 0.2$; and $\Delta [\text{C}/\text{Fe}] = \pm 0.3$) are calculated from the internal FERRE statistical errors combined with the systematics estimated in Aguado et al. (2017b).

In Fig. 3 we show the OSIRIS spectra from our sample of EMP candidates (black lines) and the best fit derived with FERRE, color-coded by temperature with blue indicating warmer and red cooler. The high quality of the OSIRIS data together with the clear CH absorptions in the G-band make it possible to derive carbon abundances and accurate metallicities in the majority of the cases.

For the star J1313–0019 we derive $T_{\text{eff}} = 5294 \pm 120$ K, in good agreement with the values inferred by Allende Prieto et al. (2015b); Frebel et al. (2015). The best value for gravity is on the edge of the grid ($\log g = 1.0 \pm 0.6$) while the preferred value from the cited original works is $\log g = 2.6$. Additionally, Aguado et al. (2017b) obtained $\log g = 3.6$ from a low-resolution ISIS² spectrum. The most likely reason FERRE drifts to a lower gravity is due to limited spectral information, given the shorter spectral range in the blue side for the OSIRIS data. Both the ISIS and BOSS³ spectrographs provide up to 15 nm wider coverage and include some Balmer lines with relevant information to derive gravity.

The impact of this deviation in T_{eff} and $[\text{Fe}/\text{H}]$ is small, and our result, $[\text{Fe}/\text{H}] = -5.03 \pm 0.2$, is slightly lower than that of Aguado et al. (2017b), $[\text{Fe}/\text{H}] = -4.7$, due the ~ 200 K difference in temperature. On the other hand, our inferred metallicity is consistent with those from Frebel et al. (2015), derived from Fe I lines observed with the MIKE⁴ spectrograph on the Magellan telescope.

Finally, the amount of carbon FERRE derives, $[\text{C}/\text{Fe}] = 3.77 \pm 0.3$, is larger than the $[\text{C}/\text{Fe}] = 2.96$ reported by Frebel et al. (2015). Such a difference is explained by the higher temperature (by 200 K), which enhances CH dissociation and the inferred carbon abundance, and the lower surface gravity we derive from the low-resolution spectrum. The impact of $\log g$ deviations when measuring carbon from low-resolution spectroscopy was deeply studied in Aguado et al. (2019b) and tends to increase the amount of carbon when the gravity is underestimated, consistent with what we find. If we force FERRE to include $\log g = 2.6$ then we recover the same $[\text{C}/\text{Fe}]$ ratio.

5. RESULTS FROM THE DESI PIPELINES

All DESI data are reduced by a pipeline that performs wavelength calibration, flatfielding, and spectral extraction accounting for the 2D shape of the PSF, flux calibration, fiber cross-talk correction, combination of multiple exposures, and

² Intermediate-dispersion Spectrograph and Imaging System

³ Baryon Oscillation Spectroscopic Survey

⁴ Magellan Inamori Kyocera Echelle

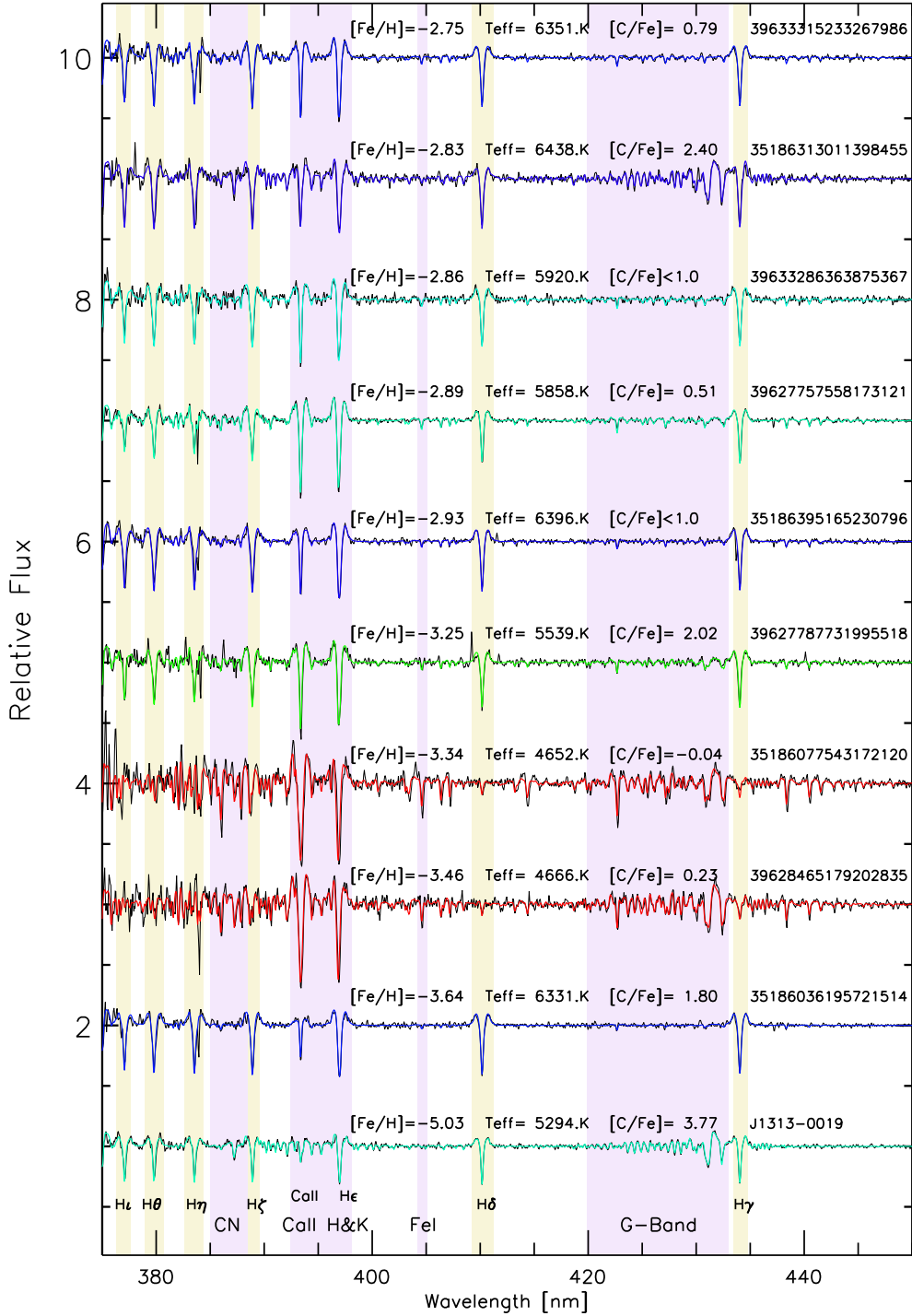


Figure 3. OSIRIS/GTC spectra (3750–4500 Å) of our stellar sample (black lines) and the best fits calculated with FERRE, colour-coded by T_{eff} (the bluer the hotter) and sorted by decreasing $[\text{Fe}/\text{H}]$. The Balmer lines (yellow) and main metallic absorptions (purple) are highlighted. Above each spectrum the metallicity, effective temperature and carbon ratios are displayed. We also show the OSIRIS spectrum of SDSS J1313-0019 for comparison.

spectral classification and redshift/radial velocity determination (Guy et al. 2023).

The stellar spectra are also processed by three pipelines developed by the Milky Way Survey working group to determine stellar radial velocities, atmospheric parameters and chemical abundances: the RVS, SP, and WD pipelines (Cooper et al. 2023). The RVS pipeline derives radial velocities and atmospheric parameters (T_{eff}), $\log g$, [Fe/H] and [a/Fe] using the RVSPEC code (Koposov 2019), based on Phoenix models (Husser et al. 2013). Similarly, the SP pipeline derives atmospheric parameters and the abundances of several individual elements by means of the FERRE code (Allende Prieto et al. 2006b). We should note that FERRE is the code adopted for the analysis of GTC spectra, however, the configuration chosen and actual models adopted differ between the two analyses. The WD pipeline is focused on the classification and the determination of the atmospheric parameters (T_{eff} and $\log g$) of white dwarfs.

The DESI reduction pipeline is continuously being improved, and several internal data releases have been produced which are named after mountains or mountain ranges: *Andes*, *Blanc*, *Cascades*, *Denali*, *Everest*, *Fuji*. *Fuji* has been tagged for public liberation in the Early Data Release (DESI et al., in prep.) and contains commissioning and survey validation observations. The Milky Way Survey pipelines have also been evolving with these internal data releases, and we present the resulting analyses for each release in Table 2. We have disregarded the *andes* and *cascade* releases from our discussion since we did not have results from both the SP and RVS pipelines for them.

Since the stars chosen for follow-up observations with GTC were all observed in the DESI commissioning, and some of the data were affected by issues that limited the instrument performance, all of them appear in the catalogs from the early data sets (e.g. *Blanc*) but some are missing in the newer ones, which only include those reobserved after commissioning. In our analysis we have only considered coadded spectra from any given program. Individual exposures taken within a survey/program pair (e.g. Survey Validation 1, 2 or 3; and the Backup program) were coadded, but data from different survey/program pairs analyzed independently. We further averaged multiple results obtained for any given star, reducing them down to a single entry per star in Table 2.

6. RESULTS AND DISCUSSION

A quick inspection of Figs. 1 and 2 reveals that the DESI observations span a significant range in signal-to-noise ratio. This happens naturally due to the broad magnitude range and single-valued effective exposure times (Guy et al. 2023) for the entire focal plane, but also due to the existence of multiple programs that take stellar spectra (dark time observa-

tions, Milky Way Survey, Backup program, etc.). Changing observing conditions are an additional source of spread in signal-to-noise ratios, but the use of an exposure-meter mitigates this effect.

The follow-up data taken at GTC and illustrated in Fig. 3 have substantially higher signal-to-noise ratios. One should also bear in mind that the analysis of both DESI and the OSIRIS observations suffer from similar theoretical shortcomings when it comes to producing accurate atmospheric parameters and abundances, such as departures from local thermodynamical equilibrium and hydrostatic equilibrium (Nordlund et al. 2009; Allende Prieto 2016), as well as uncertainties in the atomic/molecular data or other systematics affecting the construction of the model atmospheres adopted. These issues are necessarily left out of the comparison, with the hope and expectation that they will not prevent us from confirming that DESI data can deliver observations free from systematic errors, at least at the same level as other existing state-of-the-art instruments.

6.1. Atmospheric parameters

Looking at the results in Table 2 and comparing with the reference atmospheric parameters included in Table 1 it is apparent that the early (*Blanc*) results for some of the targets, notably target ID 39633315233267986, were fairly discrepant from those obtained in the more recent versions, which are better aligned with the reference values. This is likely related to a number of improvements made in the data reduction pipeline after *Blanc*.

Table 3 shows the mean and standard deviation of the differences between the various results from the DESI pipelines and data releases, and those obtained from the analysis of the OSIRIS data. The DESI spectrographs are fiber-fed and rest in a temperature-controlled room. Furthermore, the presence of prominent telluric lines in the wide DESI spectral range allows for a determination of possible zero points. On the other hand, OSIRIS was mounted on the rotating Nasmyth-B focus of the GTC, subject to variable forces and temperatures. (Since then the instrument has been moved to the Cassegrain focus, but the same caveats hold). The velocities from DESI are the reference here and the significant variations found are expected and attributed to systematics in the OSIRIS data. Therefore, for clarity, radial velocities are not included in the comparison in Table 3.

The atmospheric parameters from DESI and OSIRIS show significant discrepancies in the oldest data release considered (*Blanc*), but then fairly good agreement in all the following ones. This is likely due to i) the removal of commissioning observations for internal data releases after *Blanc*, and ii) the evolution of the software in the pipelines, both in the data reduction pipeline as well as in the Milky Way Survey RVS and SP stellar analysis pipelines.

Name	OSIRIS			Blanc			Denali			Everest			Fuji		
	Teff	logg	[Fe/H]	Teff	logg	[Fe/H]	Teff	logg	[Fe/H]	Teff	logg	[Fe/H]	Teff	logg	[Fe/H]
RVS															
39627757558173121	5857	5.0	-2.89	5935	4.82	-3.00	5938	4.85	-2.97	5848	4.70	-3.04	5842	4.57	-2.86
39627787731995518	5538	1.0	-3.25	6138	4.84	-2.69	6167	4.66	-2.91	6181	4.78	-2.68	6162	4.80	-2.67
35186036195721514	6331	5.0	-3.64	6484	4.44	-4.00
35186077543172120	4652	5.0	-3.34	4764	4.63	-2.89
35186313011398455	6438	5.0	-2.83	6249	4.38	-2.25
35186395165230796	6395	5.0	-2.93	6513	4.85	-3.00
39628465179202835	4666	4.2	-3.46	4811	4.06	-3.00	5071	5.93	-3.05	4812	4.41	-3.03
39633286363875367	5920	3.8	-2.86	6281	4.65	-3.02	6444	5.00	-2.60	6348	4.78	-2.62	6378	4.78	-2.58
39633315233267986	6351	5.0	-2.75	8190	3.78	-2.10	6563	4.97	-2.46	6463	4.78	-2.67	6441	4.72	-2.69
SP															
39627757558173121	5857	5.0	-2.89	5942	5.00	-2.85	5841	5.00	-2.99	5819	4.65	-3.22	5822	4.81	-2.99
39627787731995518	5538	1.0	-3.25	6000	4.87	-2.75	6189	4.99	-2.68	6122	4.79	-2.65	6115	4.77	-2.65
35186036195721514	6331	5.0	-3.64	6508	4.65	-3.68
35186077543172120	4652	5.0	-3.34	4636	4.94	-2.93
35186313011398455	6438	5.0	-2.83	6325	4.38	-3.05
35186395165230796	6395	5.0	-2.93	6385	4.77	-2.93
39628465179202835	4666	4.2	-3.46	4460	4.17	-3.48	4743	5.00	-3.11	4790	4.91	-3.04
39633286363875367	5920	3.8	-2.86	5694	4.16	-1.66	6342	4.89	-2.60	6336	4.84	-2.72	6360	4.84	-2.56
39633315233267986	6351	5.0	-2.75	5513	3.99	-2.45	6456	4.84	-2.62	6421	4.81	-2.81	6418	4.79	-2.80

Table 2. Atmospheric parameters derived by the DESI Milky Way Survey RVS and SP pipelines for various data releases. The missing data are related to commissioning observations not processed as part of internal data releases after *Blanc*. The parameters derived from the OSIRIS spectra are copied from Table 1 for reference.

dataset	pipeline	Nstars	$\langle \Delta T_{\text{eff}} \rangle$	$\sigma(T_{\text{eff}})$	$\langle \Delta \log g \rangle$	$\sigma(\log g)$	$\langle \Delta [\text{Fe}/\text{H}] \rangle$	$\sigma(\text{Fe})$
			K	K	cm s ⁻²	cm s ⁻²	dex	dex
Blanc	RVS	9	265.42	581.77	-0.44	0.37	0.15	0.35
Blanc	SP	9	-168.23	284.25	-0.39	0.31	0.17	0.38
Denali	RVS	4	209.10	101.65	-0.03	0.26	0.09	0.18
Denali	SP	4	137.98	92.94	0.02	0.16	0.10	0.14
Everest	RVS	5	170.74	101.30	0.10	0.53	0.12	0.17
Everest	SP	5	76.54	104.39	-0.07	0.23	0.03	0.22
Fuji	RVS	5	115.26	102.31	-0.23	0.21	0.17	0.12
Fuji	SP	5	89.52	102.32	-0.07	0.18	0.13	0.18

Table 3. Statistics (mean and standard deviation) for the differences between the parameters derived from various data releases and pipelines (RVS or SP) with respect to those obtained for the same stars from the OSIRIS observations. Going down in the table leads to more recent data sets.

The most relevant statistics for our study are the most recent ones, those corresponding to *Fuji* –the data to be released in the near future as part of the DESI Early Data Release. These results indicate that there is good agreement, with small zero-point differences and modest scatter, both at the level of 100 K for T_{eff} , and < 0.2 dex for $\log g$ as well as $[\text{Fe}/\text{H}]$. This is true for both the RVS and SP pipelines.

The low scatter is smaller than the uncertainties expected for the OSIRIS observations (the latter are 120 K for T_{eff} ,

0.6 dex for $\log g$ and 0.2 dex for $[\text{Fe}/\text{H}]$), however the expected uncertainties include an estimate of systematic errors due to the approximations involved in the analysis, and some of these cancel out in the statistics given that they apply to both the analysis of the OSIRIS and DESI spectra. In addition, all the DESI targets considered in this study appear to be dwarf stars, which may hide systematic errors affecting giants, such as those discussed in §4 for J1313–0019.

6.2. Elemental abundances

The most recent version of the SP pipeline, which was run on the *Fuji* data release, includes a preliminary determination of individual abundances (C, Mg, Ca and Fe), and therefore we have estimates of the carbon and iron abundances for the stars under study from DESI spectra. The analysis uses the same model spectra as for the derivation of atmospheric parameters, but for any given element the main atmospheric parameters are frozen and only one parameter ($[\alpha/\text{Fe}]$ for α elements, or $[\text{Fe}/\text{H}]$ for the rest of the elements) is searched, computing the χ^2 using only sections of the spectra dominated by transitions involving that element: atomic transitions or those of a molecule that includes that element. Such a scheme has been successfully adopted for the APOGEE survey (García Pérez et al. 2016; Majewski et al. 2017).

We should stress that the iron abundances derived in this manner are fundamentally different from the overall metallicity (also named $[\text{Fe}/\text{H}]$) discussed in previous sections. The overall metallicity is determined from lines of all *metals*, i.e. all elements with atomic number higher than 2. Despite that iron being the element that contributes most line absorption for most late-type stars, other elements have a non-negligible weight when performing these measurements. On the other hand, the iron abundance discussed in this section is derived almost exclusively from the strength of iron lines, to the extent that they are unblended with other features. In a sense the iron abundances derived in this manner can be considered a more pure measurement and should be more representative of the actual iron abundances in these stars.

Figure 4 illustrates the position of the targets in the $[\text{C}/\text{Fe}]$ vs. $[\text{Fe}/\text{H}]$ plane, based on the OSIRIS data. Two groups are visible in this plot, one with carbon-to-iron values at the level of about $[\text{C}/\text{Fe}] \sim 2$, and another with lower values ($[\text{C}/\text{Fe}] < 1$). The increasing relative carbon enhancement at lower metallicity is considered as the signature of mixing and fall-back in the supernovae explosions of the first generation of metal-free stars (Umeda & Nomoto 2003). The stars with lower $[\text{C}/\text{Fe}]$ in Fig. 4 are not necessarily inconsistent with this picture, since the mass range for the progenitors and the stochastic nature of the mixing and fall-back processes may naturally lead to a large spread in carbon abundances (Bonifacio et al. 2015). Chiaki et al. (2015) have modeled the formation of the first stars considering the effect of dust cooling in the protostellar cloud, and concluded that it is not possible to form low-mass stars in the region highlighted in Fig. 4. The sample of stars currently available is consistent with that regime, but the statistics are poor and DESI can play an important role to enlarge the numbers of extremely metal-poor stars with carbon determinations.

The $[\text{C}/\text{Fe}]$ values returned by the SP pipeline, however, do not show an agreement nearly as good as that found for the $[\text{Fe}/\text{H}]$ in Table 2 for the same data release (*Fuji*). While

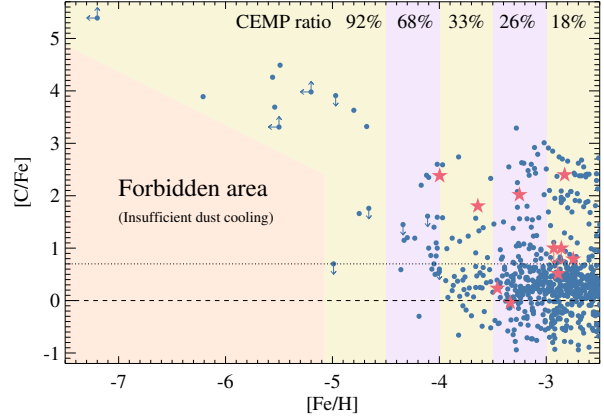


Figure 4. Carbon-to-iron ratio vs. iron abundance in the ten stars from our sample (red stars) together with metal-poor stars with carbon abundances from the JINA database (blue circles; Abohalima & Frebel 2018). We also include the 14 known stars already known in the $[\text{Fe}/\text{H}] < -4.5$ regime Christlieb et al. (2004); Frebel et al. (2005); Norris et al. (2007); Caffau et al. (2011); Hansen et al. (2014); Keller et al. (2014); Allende Prieto et al. (2015b); Bonifacio et al. (2015); Caffau et al. (2016); Aguado et al. (2018b,a, 2019a); Nordlander et al. (2019); González Hernández et al. (2020). The fraction of carbon-enhanced metal-poor stars (CEMPs) in each regime are also shown.

the approximate methodology adopted is expected to break down for large deviations from the $[\text{C}/\text{Fe}] = 0$ value adopted in the construction of the model grids, the reasons for the discrepancies found are of a different nature.

Early on during the commissioning of DESI it was found that the blue collimators of the DESI spectrographs have an imperfection in their coatings that induces an optical artifact around 430 nm. The exact wavelength and the actual distortions induced in the spectra vary from collimator to collimator and somewhat as a function of time. An example of this affection can be clearly seen in the middle-left panel of Figure 2. This issue makes it difficult to use DESI spectra to infer carbon abundances from the CH band at 430 nm, which is the main feature used to measure the abundance of this element in medium resolution optical spectra. Fortunately, the DESI collimators are being replaced by others with identical properties but without the 430 nm artifact.

The $[\text{Fe}/\text{H}]$ values obtained with the same methodology agree quite well with the OSIRIS determinations with a mean difference of 0.04 and a standard deviation of 0.14 dex, to be compared with a mean difference of 0.13 and a standard deviation of 0.18 dex found for the *Fuji* SP DESI $[\text{Fe}/\text{H}]$ global-parameter determinations.

We cannot use the OSIRIS observations to evaluate the abundances of Mg and Ca from DESI spectra. The OSIRIS observations do not offer useful Mg transitions that can be used to derived the abundance of this element. In addition, as

explained in Section 4.2, a constant abundance ratio $[\alpha/\text{Fe}]$ is assumed in the analysis of the OSIRIS data, which couples strongly the inferred metallicity to the strength of the Ca II H and K lines.

7. CONCLUSION

In this paper we report on the analysis of observations taken with the OSIRIS spectrograph at the 10.4m GTC of a sample metal-poor stars observed by DESI. The OSIRIS data have lower spectral resolution and shorter wavelength coverage than those offered by DESI, but a much higher signal-to-noise ratio and benefit from a well-vetted data treatment and analysis methodology customized for metal-poor stars.

The targets under consideration were chosen for being part of the DESI commissioning observations, which in some cases included some shortcomings or issues, but some of the targets have been since reobserved by DESI. The DESI data analysis pipelines have been evolving continuously since the instrument started operations, and therefore multiple data releases, corresponding to several observing periods, programs and versions of the data processing software, have been considered.

We find very good agreement between the atmospheric parameters derived from DESI and OSIRIS data. In the most recent incarnation of the DESI data, soon-to-be released as the DESI Early Data Release, the inferred values of the stellar T_{eff} , $\log g$ and $[\text{Fe}/\text{H}]$ agree with the determinations from OSIRIS data to better than about 100 K, 0.2 dex and 0.2 dex, respectively. This applies to both random and systematic errors, although some of the latter may hide as they are shared by the analysis of both the DESI and OSIRIS data. The results from the two DESI Milky Way Survey pipelines, the SP and RVS branches, agree fairly well, and therefore our conclusion applies to both.

The preliminary values of abundances of individual elements provided by the DESI SP pipeline appear to be promising, judging from the iron abundances obtained for these metal-poor stars. The abundances of $[\text{Fe}/\text{H}]$ show excellent agreement with the OSIRIS values (mean difference of 0.04 dex and a standard deviation of 0.14 dex), with even higher consistency with them than the metallicities obtained in the global simultaneous fitting of all atmospheric parameters. Although we also have carbon abundances from the OSIRIS spectra, those from DESI exhibit significant discrepancies, which we associate with an artifact introduced at 430 nm by the DESI collimators, which makes it difficult to derive reliable carbon abundances from the CH band at the same wavelengths. The collimators are progressively being replaced, and that will solve this issue for future DESI observations.

ACKNOWLEDGMENTS

Based on observations made with the Gran Telescopio Canarias (GTC), installed at the Spanish Observatorio del Roque de los Muchachos of the Instituto de Astrofísica de Canarias, on the island of La Palma.

CAP, JIGH and RR acknowledge financial support from the Spanish Ministry MICINN projects AYA2017-86389-P and PID2020-117493GB-I00. Partial help was received from the program Unidad de Excelencia María de Maeztu CEX2020-001058-M. This research made use of computing time available on the high-performance computing systems at the Instituto de Astrofísica de Canarias. DA acknowledge support from the European Research Council (ERC) Starting Grant NEFERTITI H2020/808240. DA also acknowledges financial support from the Spanish Ministry of Science and Innovation (MICINN) under the 2021 Ramón y Cajal program MICINN RYC2021-032609. The authors thankfully acknowledge the technical expertise and assistance provided by the Spanish Supercomputing Network (Red Española de Supercomputación), as well as the computer resources used: the LaPalma Supercomputer and the Diva cluster, both located at the Instituto de Astrofísica de Canarias. We have made extensive use of the software from astropy (Astropy Collaboration et al. 2022).

This material is based upon work supported by the U.S. Department of Energy (DOE), Office of Science, Office of High-Energy Physics, under Contract No. DE-AC02-05CH11231, and by the National Energy Research Scientific Computing Center, a DOE Office of Science User Facility under the same contract. Additional support for DESI was provided by the U.S. National Science Foundation (NSF), Division of Astronomical Sciences under Contract No. AST-0950945 to the NSF's National Optical-Infrared Astronomy Research Laboratory; the Science and Technologies Facilities Council of the United Kingdom; the Gordon and Betty Moore Foundation; the Heising-Simons Foundation; the French Alternative Energies and Atomic Energy Commission (CEA); the National Council of Science and Technology of Mexico (CONACYT); the Ministry of Science and Innovation of Spain (MICINN), and by the DESI Member Institutions: <https://www.desi.lbl.gov/collaborating-institutions>. Any opinions, findings, and conclusions or recommendations expressed in this material are those of the author(s) and do not necessarily reflect the views of the U. S. National Science Foundation, the U. S. Department of Energy, or any of the listed funding agencies.

This work has made use of data from the European Space Agency (ESA) mission Gaia (<https://www.cosmos.esa.int/gaia>), processed by the Gaia Data Processing and Analysis Consortium (DPAC, <https://www.cosmos.esa.int/webgaiadpacconsortium>). Funding for the DPAC has been provided by national institutions, in particular the institutions participating in the Gaia Multilateral Agreement.

The authors are honored to be permitted to conduct scientific research on Iolkam Du'ag (Kitt Peak), a mountain with particular significance to the Tohono O'odham Nation.

For more information, visit desi.lbl.gov

All the data used in the figures are available from <https://zenodo.org/deposit/8020841>

Software: NumPy (Harris et al. 2020), SciPy (Virtanen et al. 2020), Astropy (Astropy Collaboration et

al. 2013, 2018), Matplotlib (Hunter 2007), PyGaia (A. Brown; Gaia Project Scientist Support Team and the Gaia DPAC; <https://github.com/agabrown/PyGaia>), galstreams (Mateu 2017).

Facilities: ORM: GTC (OSIRIS), KPNO:Mayall (Mosaic3), Steward:Bok (90Prime), CTIO:Blanco (DECam), WISE, Gaia.

REFERENCES

Abohalima, A., & Frebel, A. 2018, *ApJS*, 238, 36

Aguado, D. S., Allende Prieto, C., González Hernández, J. I., et al. 2016, *A&A*, 593, A10

Aguado, D. S., Allende Prieto, C., González Hernández, J. I., & Rebolo, R. 2018a, *ApJL*, 854, L34

Aguado, D. S., Allende Prieto, C., González Hernández, J. I., Rebolo, R., & Caffau, E. 2017a, *A&A*, 604, A9

Aguado, D. S., González Hernández, J. I., Allende Prieto, C., & Rebolo, R. 2017b, *A&A*, 605, A40

—. 2018b, *ApJL*, 852 L20, doi:10.1086/498131

—. 2019a, *ApJL*, 874, L21

Aguado, D. S., Youakim, K., González Hernández, J. I., et al. 2019b, *MNRAS*, 490, 2241

Aguado, D. S., Molaro, P., Caffau, E., et al. 2022, *A&A*, 668, A86

Alexander, D. M., Davis, T. M., Chaussidon, E., et al. 2022, arXiv e-prints, arXiv:2208.08517

Allende Prieto, C. 2016, *Living Reviews in Solar Physics*, 13, 1

—. 2021, *Nature Astronomy*, 5, 105

Allende Prieto, C., Beers, T. C., Wilhelm, R., et al. 2006a, *ApJ*, 636, 804

—. 2006b, *ApJ*, 636, 804

Allende Prieto, C., Fernández-Alvar, E., Aguado, D. S., et al. 2015a, *A&A*, 579, A98

—. 2015b, *A&A*, 579, A98

Allende Prieto, C., Cooper, A. P., Dey, A., et al. 2020, *Research Notes of the American Astronomical Society*, 4, 188

Arentsen, A., Aguado, D. S., Sestito, F., et al. 2023, *MNRAS*, 519, 5554

Arentsen, A., Starkenburg, E., Martin, N. F., et al. 2020, *MNRAS*, 496, 4964

Astropy Collaboration, Price-Whelan, A. M., Lim, P. L., et al. 2022, *ApJ*, 935, 167

Bailey et al. 2023, in preparation

Bertran de Lis, S., Allende Prieto, C., Majewski, S. R., et al. 2016, *A&A*, 590, A74

Boender, C. G. E., Rinnoy Kan, A. H. G., Timmer, G. T., & Stougie, L. 1982, *Mathematical Programming*, 22, 125

Bonifacio, P., Caffau, E., Spite, M., et al. 2015, *A&A*, 579, A28

Bromm, V., & Larson, R. B. 2004, *ARA&A*, 42, 79

Bromm, V., & Loeb, A. 2003, *Nature*, 425, 812

Buder, S., Sharma, S., Kos, J., et al. 2020, arXiv e-prints, arXiv:2011.02505

Caffau, E., Bonifacio, P., François, P., et al. 2011, *Nature*, 477, 67

Caffau, E., Bonifacio, P., Spite, M., et al. 2016, *A&A*, 595, L6

Cepa, J. 2010, in *Astrophysics and Space Science Proceedings*, Vol. 14, *Highlights of Spanish Astrophysics V*, 15

Chaussidon, E., Yèche, C., Palanque-Delabrouille, N., et al. 2023, *ApJ*, 944, 107

Chen, L.-H., Pillepich, A., Glover, S. C. O., & Klessen, R. S. 2023, *MNRAS*, 519, 483

Chiaki, G., Marassi, S., Nozawa, T., et al. 2015, *MNRAS*, 446, 2659

Christlieb, N., Gustafsson, B., Korn, A. J., et al. 2004, *ApJ*, 603, 708

Clark, P. C., Glover, S. C. O., Smith, R. J., et al. 2011, *Science*, 331, 1040

Cooper, A. P., Koposov, S. E., Allende Prieto, C., et al. 2023, *ApJ*, 947, 37

Cui, X.-Q., Zhao, Y.-H., Chu, Y.-Q., et al. 2012, *Research in Astronomy and Astrophysics*, 12, 1197

Da Costa, G. S., Bessell, M. S., Nordlander, T., et al. 2022, arXiv e-prints, arXiv:2210.05161

de Jong, R. S., Bellido-Tirado, O., Brynnel, J. G., et al. 2022, in *Society of Photo-Optical Instrumentation Engineers (SPIE) Conference Series*, Vol. 12184, *Ground-based and Airborne Instrumentation for Astronomy IX*, ed. C. J. Evans, J. J. Bryant, & K. Motohara, 1218414

DESI Collaboration, Aghamousa, A., Aguilar, J., et al. 2016a, arXiv e-prints, arXiv:1611.00036

—. 2016b, arXiv e-prints, arXiv:1611.00037

DESI Collaboration, Abareshi, B., Aguilar, J., et al. 2022a, arXiv e-prints, arXiv:2205.10939

—. 2022b, *AJ*, 164, 207

DESI collaboration et al. 2023, in preparation

Dey, A., Schlegel, D. J., Lang, D., et al. 2019, *AJ*, 157, 168

Frebel, A., Chiti, A., Ji, A. P., Jacobson, H. R., & Placco, V. M. 2015, *ApJL*, 810, L27

Frebel, A., Christlieb, N., Norris, J. E., et al. 2007, *ApJL*, 660, L117

Frebel, A., Aoki, W., Christlieb, N., et al. 2005, *Nature*, 434, 871

Gaia Collaboration, Vallenari, A., Brown, A. G. A., et al. 2022, arXiv e-prints, arXiv:2208.00211

García Pérez, A. E., Allende Prieto, C., Holtzman, J. A., et al. 2016, *AJ*, 151, 144

González Hernández, J. I., Aguado, D. S., Allende Prieto, C., Burgasser, A. J., & Rebolo, R. 2020, *ApJL*, 889, L13

Górski, K. M., & et al. 1999, in *Evolution of Large Scale Structure : From Recombination to Garching*, ed. A. J. Banday, R. K. Sheth, & L. N. da Costa, 37

Greif, T. H., Springel, V., White, S. D. M., et al. 2011, *ApJ*, 737, 75

Guy et al. 2023, in preparation

Hahn, C., Wilson, M. J., Ruiz-Macías, O., et al. 2022, arXiv e-prints, arXiv:2208.08512

Hansen, T., Hansen, C. J., Christlieb, N., et al. 2014, *ApJ*, 787, 162

Husser, T. O., Wende-von Berg, S., Dreizler, S., et al. 2013, *A&A*, 553, A6

Iwamoto, N., Umeda, H., Tominaga, N., Nomoto, K., & Maeda, K. 2005, *Science*, 309, 451

Jin, S., Trager, S. C., Dalton, G. B., et al. 2022, arXiv e-prints, arXiv:2212.03981

Joggerst, C. C., Woosley, S. E., & Heger, A. 2009, *ApJ*, 693, 1780

Keller, S. C., Bessell, M. S., Frebel, A., et al. 2014, *Nature*, 506, 463

Koesterke, L., Allende Prieto, C., & Lambert, D. L. 2008, *ApJ*, 680, 764

Koposov, S. E. 2019, RVSpecFit: Radial velocity and stellar atmospheric parameter fitting, *Astrophysics Source Code Library*, record ascl:1907.013, , ascl:1907.013

Kunder, A., Kordopatis, G., Steinmetz, M., et al. 2017, *AJ*, 153, 75

Lan, T.-W., Tojeiro, R., Armengaud, E., et al. 2022, arXiv e-prints, arXiv:2208.08516

Levi, M., Bebek, C., Beers, T., et al. 2013, arXiv e-prints, arXiv:1308.0847

Majewski, S. R., Schiavon, R. P., Frinchaboy, P. M., et al. 2017, *AJ*, 154, 94

Mészáros, S., Allende Prieto, C., Edvardsson, B., et al. 2012, *AJ*, 144, 120

Miller et al. 2022, in preparation

Moustakas et al. 2022, in preparation

Nordlander, T., Bessell, M. S., Da Costa, G. S., et al. 2019, *MNRAS*, 488, L109

Nordlund, Å., Stein, R. F., & Asplund, M. 2009, *Living Reviews in Solar Physics*, 6, 2

Norris, J. E., Christlieb, N., Korn, A. J., et al. 2007, *ApJ*, 670, 774

Norris, J. E., Bessell, M. S., Yong, D., et al. 2013, *ApJ*, 762, 25

Raichoor, A., Eisenstein, D. J., Karim, T., et al. 2020, *Research Notes of the American Astronomical Society*, 4, 180

Raichoor, A., Moustakas, J., Newman, J. A., et al. 2023, *AJ*, 165, 126

Ruiz-Macías, O., Zarrouk, P., Cole, S., et al. 2020, *Research Notes of the American Astronomical Society*, 4, 187

Schlaflay et al. 2023, in preparation

Schlegel et al. 2023, in preparation

Silber, J. H., Fagrelius, P., Fanning, K., et al. 2023, *AJ*, 165, 9

Stacy, A., & Bromm, V. 2014, *ApJ*, 785, 73

Stacy, A., Bromm, V., & Lee, A. T. 2016, *MNRAS*, 462, 1307

Starkenburg, E., Oman, K. A., Navarro, J. F., et al. 2017, *MNRAS*, 465, 2212

Starkenburg, E., Aguado, D. S., Bonifacio, P., et al. 2018, *MNRAS*, 481, 3838

Umeda, H., & Nomoto, K. 2003, *Nature*, 422, 871

Yèche, C., Palanque-Delabrouille, N., Claveau, C.-A., et al. 2020, *Research Notes of the American Astronomical Society*, 4, 179

York, D. G., Adelman, J., Anderson, John E., J., et al. 2000, *AJ*, 120, 1579

Zhou, R., Newman, J. A., Dawson, K. S., et al. 2020, *Research Notes of the American Astronomical Society*, 4, 181

Zhou, R., Dey, B., Newman, J. A., et al. 2023, *AJ*, 165, 58

Zou, H., Zhou, X., Fan, X., et al. 2017, *PASP*, 129, 064101